

Fig. 4. (A) Experimental distribution of P_e over a dot-shape ensemble of ~ 200 independent samples, compared with random matrix theory. Statistics for P_e are based on the value $P_c = 0.7$ extracted for this device. (B) Examples of polarization fluctuations as a function of V_g for three different dot shapes.

spacing, zero temperature, and zero dephasing rate (10). This model gives a probability density for the spin polarization of current of the form $P(p) = 1/(1+|p|)^2$, with zero average and typical fluctuations (standard deviation) $\sigma(p) = 0.48$. Using the value of P_e determined above, the experimental value is $\sigma(p) = 0.27 \pm 0.06$.

It is not surprising that $\sigma(p)$ is overestimated by a zero-temperature theory. One may compare the reduction factor (relative to zero-temperature theory) for typical fluctuations of spin polarization with the analogous factor for conductance fluctuations. Conductance fluctuations measured simultaneously in the emitter dot gave $\sigma(g) = 0.21 \pm 0.02 e^2/h$, which is 51% of the theoretical zero-temperature UCF value for single-mode leads (8), accounting for lifted spin degeneracy. This is consistent with the reduction factor $0.27/0.48 = 56\%$ observed for spin polarization. Despite the reduction factor, spin polarizations up to $\sim 70\%$ are readily obtained.

In summary, we have realized a quantum coherent spin filter based on interference in an open quantum dot, and we have measured its properties in a polarizer-analyzer geometry. Although the filtering properties of the dot require

phase coherence within the dot, the resulting spin polarized current will remain polarized upon exiting the dot up to the spin relaxation time, which in practice may greatly exceed the phase coherence time. We find reasonable agreement between measured spin polarization statistics and a random matrix theory model. However, a fully developed theory of mesoscopic fluctuations of spin current is not yet in hand.

References and Notes

1. F. J. Jedema et al., *Nature* **416**, 713 (2002).
2. P. R. Hammar, M. Johnson, *Phys. Rev. Lett.* **88**, 066806 (2002).
3. R. Fiederling et al., *Nature* **402**, 787 (1999).
4. Y. Ohno et al., *Nature* **402**, 790 (1999).
5. A. S. Sachrajda et al., *Physica E* **10**, 493 (2001).
6. R. M. Potok et al., *Phys. Rev. Lett.* **89**, 266602 (2002).
7. C. W. J. Beenakker, *Rev. Mod. Phys.* **69**, 731 (1997).
8. H. van Houten et al., *Phys. Rev. B* **39**, 8556 (1989).
9. I. H. Chan et al., *Phys. Rev. Lett.* **74**, 3876 (1995).
10. P. W. Brouwer, unpublished work.
11. We thank P. Brouwer for valuable contributions. This work was supported by the DARPA QuIST (Defense Advanced Research Projects Agency Quantum Information Science and Technology) Program and Army Research Office (ARO) under DAAD19-01-1-0659. J.A.F. acknowledges support from a Stanford Graduate Fellowship. R.M.P. acknowledges support as an ARO Graduate Research Fellow.

13 September 2002; accepted 23 December 2002

Zero-Mode Waveguides for Single-Molecule Analysis at High Concentrations

M. J. Levene,¹ J. Korch,^{1,2} S. W. Turner,^{1,*} M. Foquet,¹ H. G. Craighead,¹ W. W. Webb^{1,†}

Optical approaches for observing the dynamics of single molecules have required pico- to nanomolar concentrations of fluorophore in order to isolate individual molecules. However, many biologically relevant processes occur at micromolar ligand concentrations, necessitating a reduction in the conventional observation volume by three orders of magnitude. We show that arrays of zero-mode waveguides consisting of subwavelength holes in a metal film provide a simple and highly parallel means for studying single-molecule dynamics at micromolar concentrations with microsecond temporal resolution. We present observations of DNA polymerase activity as an example of the effectiveness of zero-mode waveguides for performing single-molecule experiments at high concentrations.

Data from a single molecule can reveal information about kinetic processes not normally accessible by ensemble measurements, such as variances in kinetic rates, memory effects, and lifetimes of transient intermediates ($1, 2$). Single-molecule approaches to drug screening, mRNA expression profiling, single-nucleotide

polymorphism detection and DNA sequencing may also have many advantages over current techniques ($3-5$). Common approaches to studying single molecules include fluorescence correlation spectroscopy (FCS) ($6, 7$) and direct observation of sparse molecules using diffraction-limited optics ($8, 9$). These approaches provide observation volumes on the order of 0.2 fl and therefore require pico- to nanomolar concentrations of fluorophore in order to isolate individual molecules in solution (10). However, many enzymes naturally work at much higher ligand concentrations, and their Michaelis constants are often in the micro- to millimolar range

(11). Low concentrations of ligand can influence the mechanistic pathway of enzyme kinetics (e.g., by allosteric control or conformational relaxation) and alter the partitioning between multiple catalytic pathways, thus affecting turnover cycle histories and distributions (12). Working at biologically more relevant, micromolar concentrations requires reducing the observation volume by over three orders of magnitude.

In addition to requiring low concentrations of ligand, the temporal resolution of conventional approaches to single-molecule kinetics is often limited by the time it takes for molecules to diffuse out of the observation volume, usually on the order of several hundred microseconds. The temporal resolution and the upper limit of practicable concentrations would be greatly improved by reducing the effective observation volume.

Previous approaches include total internal reflection illumination, which can reduce the observation volume by a factor of 10 (13), and near-field scanning optical microscopy (NSOM), which achieves observation volumes with lateral dimensions on the order of 50 nm by illumination through a small aperture, usually terminating a tapered optical fiber (14). NSOM has been used to observe single molecules on a surface (15), but it suffers from unreliable probe manufacture and its complexity is not easily amenable to highly parallel implementations.

Concurrent to the development of single-molecule analytical techniques has been rapid progress in nanobiotechnology and efforts at

¹Applied and Engineering Physics, ²Graduate Program in Biochemistry, Molecular, and Cell Biology, Cornell University, Clark Hall, Ithaca, NY 14853, USA.

*Present address: Nanofluidics Incorporated, 17 Sheraton Drive, Ithaca, NY 14850, USA.

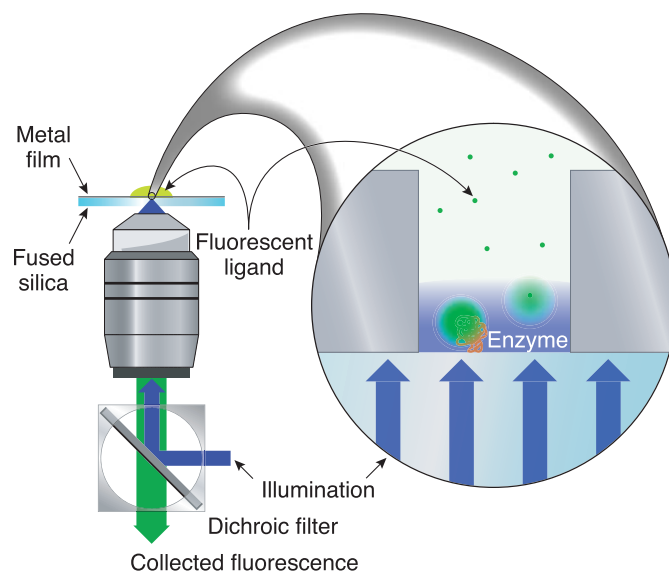
†To whom correspondence should be addressed. E-mail: www2@cornell.edu

building “lab-on-a-chip” systems for low-cost, high-throughput analytical biochemistry (16–18). Here, we demonstrate a nanostructured device, the zero-mode waveguide, for highly efficient single-molecule analysis at high fluorophore concentrations and its application to enzyme analysis.

Metal-clad waveguides exhibit a cut-off wavelength above which no propagating modes exist inside the waveguide. This cut-off wavelength is related to the shape and size of the guide. For a circular guide of diameter d clad with a perfect conductor, light will be above the cut-off wavelength, λ_c , for the lowest frequency mode, transverse mode TE_{11} , if $d \leq 0.586\lambda_m$, where λ_m is the wavelength in the medium composing the core of the waveguide (19). Longer wavelengths ($\lambda_m > \lambda_c = 1.7d$) are evanescent and their intensity, $I(z)$, decays exponentially along the length (z) of the guide as $I(z) = e^{-z/\Lambda}$, where

$$\frac{1}{\Lambda} = 2 \sqrt{\frac{1}{\lambda^2} - \frac{1}{\lambda_m^2}} \quad (1)$$

Fig. 1. An apparatus for single-molecule enzymology using zero-mode waveguides.



taining the fluorescently tagged ligand molecules. The coverslip is illuminated through a microscope objective from below, and the fluorescence is collected back through the same objective (Fig. 1). In this case, the observed signal consists of fluorescence from the ligand molecule that is in the active site of the enzyme. This signal must be distinguished from a background of freely diffusing fluorescent ligand within the waveguide's observation volume. The limited dimensions of the observation volume reduce the number of observable diffusing molecules and the correlation time of the resulting fluorescence fluctuations, allowing for easy discrimination of the signal from background.

Zero-mode waveguides can also be used for high-concentration FCS and cross-correlation experiments. Cross-correlation of the fluorescence from distinctly labeled, freely diffusing analytes is a powerful technique for monitoring binding efficiencies and for high-throughput drug screening (20, 21). As with conventional FCS, the cross-correlation technique works best with only a few molecules, on average, per observation volume. Zero-mode waveguides would therefore allow this technique to be performed at higher, more physiologically relevant concentrations.

In order to guide the design of zero-mode waveguides and to derive the shape and size of their effective observation volumes, it is necessary to know the intensity distribution inside the waveguide. For waveguides with $d \ll \lambda_m$ and real metal cladding, the skin depth has a strong effect on the solution to Maxwell's equations, and numerical solutions must be found. Hence, we have performed three-dimensional finite-element time-domain simulations of the intensity distribution within the guides (22). A cross section of the simulation results for a 50-nm-diameter waveguide is shown in Fig. 2A. We found that circularly polarized incident light provides a more uniform illumination profile across the diameter of the waveguide as compared to that of linearly polarized light. Ap-

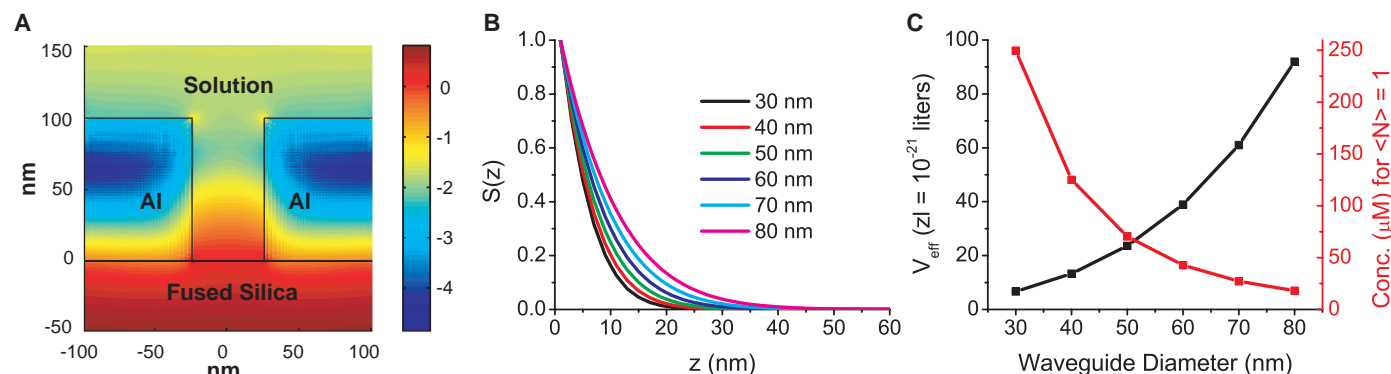


Fig. 2. (A) Three-dimensional finite-element time-domain simulation of the intensity distribution (log scale) for a zero-mode waveguide 50 nm in diameter and 100 nm long. (B) $S(z)$ curves for different waveguide diameter, d . (C) V_{eff} and the corresponding concentration for which there is, on average, one molecule in the volume ($\langle N \rangle = 1$).

REPORTS

proximating the profile as constant across the diameter of the waveguide thus reduces our analysis to a one-dimensional problem in terms of the intensity as a function of depth into the waveguide, $I(z)$.

Although the function $I(z)$ describes how effectively a fluorophore at a given depth in the waveguide is excited, the coupling of fluorescence back out of the waveguide, where it can be detected, also needs to be taken into account. Finite-element simulations of dipoles with horizontal and vertical orientations at various depths within the waveguide demonstrated coupling efficiencies that decayed exponentially with increasing dipole depth inside the guide. Appropriate averaging over all dipole orientations yields $p(z)$, the dipole coupling efficiency as a function of dipole depth in the waveguide. As with the illumination profile, the coupling efficiency was only a weak function of lateral position within the waveguide.

Kleppner (23) showed that metal-clad waveguides used at or above the cut-off wavelength can have a profound effect on radiative rates. This change in radiative rate will affect the quantum yield of the fluorophore and therefore the shape of the observation volume. In general, the radiative rate of a dipole is proportional to the density of photonic states available for emission at the appropriate frequency (24, 25). A detailed calculation of changes to the radiative rate as a function of position in zero-mode waveguides is beyond the scope of this paper. However, for our current purpose we will make the approximation that the photon density of states, and hence the radiative rate, is proportional to the output coupling from the waveguide and therefore proportional to $p(z)$. The fluorescence quantum yield, Q , is a function of the radiative and nonradiative rates of dipole de-excitation, k_r and k_{nr} , such that

$$Q(z) = \frac{k_r(z)}{k_r(z) + k_{nr}} \approx \frac{p(z)}{p(z) + C} \quad (2)$$

where C is a constant such that $Q(0)$ equals the quantum yield at the entrance of the waveguide.

Quenching by bare metal could contribute to

k_{nr} . However, any oxide layer on the metal surface, as is expected with aluminum, prevents diffusing dye from direct contact with the metal. Any quenching of dye is also likely to be independent of the depth within the waveguide and therefore would not strongly affect $Q(z)$.

The effective observation profile, $S(z)$, is therefore described by the product of the excitation and collection efficiencies and the quantum yield as a function of depth in the waveguide,

$$S(z) = I(z)p(z) \frac{p(z)}{p(z) + C} \quad (3)$$

and the effective observation volume, V_{eff} , is given by (26)

$$V_{\text{eff}} = \frac{\pi d^2}{4} \frac{(\int S(z) dz)^2}{\int S^2(z) dz} \quad (4)$$

for a waveguide of diameter d . $S(z)$ decays fast enough to limit the volume of observation to the first 10 or 20 nm into the waveguide, depending on the diameter of the guide (Fig. 2B). V_{eff} is shown as a function of d in Fig. 2C, as well as the corresponding concentration at which there is, on average, one molecule in the observation volume at any given time. Volumes as small as 10 zeptoliters, more than four orders of magnitude smaller than the diffraction limit, are possible. Thus, for the smallest waveguides it is possible to work at concentrations as high as 200 μM and still have less than one molecule per volume.

Arrays of zero-mode waveguides were manufactured as small holes in an 89-nm thick film of aluminum on fused silica coverslips (Fig. 3). Holes of various diameters were patterned with the use of electron beam lithography followed by reactive ion etching (22).

FCS was used to characterize the observation volume inside the waveguides and to demonstrate their usefulness for high-concentration FCS and cross-correlation. One-dimensional FCS curves can be derived from the profile $S(z)$ with the use of either a Fourier (27) or a Laplace (28) transform, assuming nonstick boundary conditions, resulting in the expression for the autocorrelation function $G(\tau)$

$$G(\tau) \propto \int_{v_L}^{\infty} \left(\int S(z) \cos(vz) dz \right)^2 e^{-v^2 D \tau} dv \quad (5)$$

where D is the diffusion coefficient of the fluorophore and τ is the correlation delay time. The integration over spatial frequencies, v , is conventionally taken from zero to infinity. However, in this case spatial frequencies corresponding to lengths longer than the length of the waveguide, L , are excluded, because correlations over this length scale will not be observed as molecules diffuse into the large external volume outside of the guide.

FCS curves taken with the use of the fluorescently tagged deoxycytidine triphosphate R110-dCTP (Amersham Biosciences) are shown in Fig. 4, A and B. This dye was chosen from our ongoing development of a single-molecule DNA sequencing technique. The data show good signal-to-noise characteristics. Any potential decrease in the signal-to-noise ratio due to the short diffusion time has been compensated for by the increased number of diffusion events at high concentrations. The diffusion coefficient and quantum yield of R110-dCTP were found independently to be $2.24 \times 10^{-6} \text{ cm}^2 \text{ s}^{-1}$ and 77%, respectively (22). These parameters were used to derive $G(\tau)$ for waveguides of various diameters with the assumption that the quantum yield at the entrance of the waveguide is the same as that for the freely diffusing dye. Fits to a 43-nm waveguide for various concentrations of fluorophore are shown in Fig. 4A; for comparison, a curve from a conventional, diffraction-limited volume using a dye concentration of 4 nM is also shown. Zero-mode waveguides increased the usable concentration range by well over three orders of magnitude.

The value of $G(0)$ scales as expected with concentration; however, a nonfluctuating background, B , from the large pool of highly concentrated dye on the opposite side of the waveguide can affect the measured value of $G(0)$ such that

$$G(0) = \frac{N}{(N + B)^2}$$

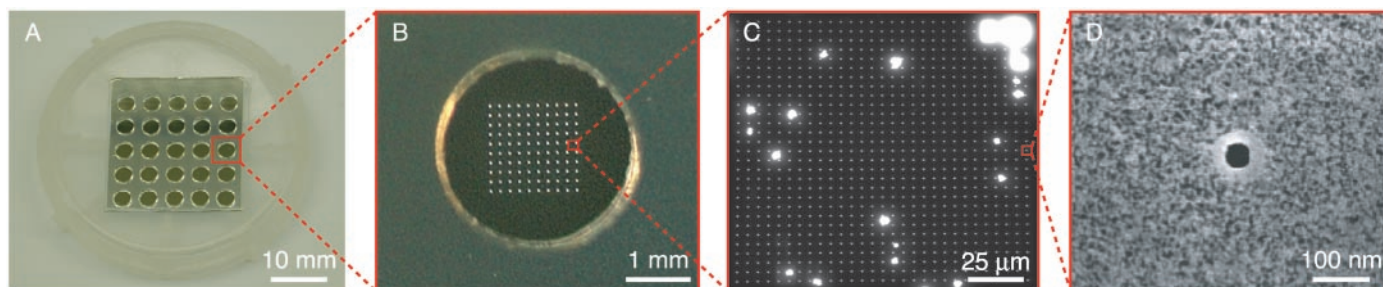


Fig. 3. A fused silica coverslip with zero-mode waveguides arrays. (A) The coverslip, with overlying gasket to isolate arrays for individual experiments. Successive increases in scale are shown in (B) to (D). A scanning

electron microscope image of an individual waveguide is shown in (D). The bright spots in (C) correspond to defects in the metal film. The large bright pattern in the upper right corner is a coded orientation marker.

where N is the average number of fluorophores in the observation volume (29). Although very little energy transmits through the waveguide in either direction, the pool of dye above the waveguides is large enough that some fluorescence will leak back through to the detector. This small fluorescence background comes from a very large number of weakly illuminated molecules and is therefore essentially constant, exhibiting negligible fluctuations. At 10 μM dye concentration, the 43-nm-diameter waveguide used for the experiments in Fig. 4A contained 0.1 molecule on average, with a corresponding background, B , equivalent to 0.18 molecule. The nonfluctuating nature of this background makes it easy to discriminate against the signal from either a millisecond-scale enzymatic event or a microsecond-scale diffusion event.

Zero-mode waveguides have excellent temporal resolution (Fig. 4B). Normalized FCS curves for 43-nm and 66-nm waveguides, along

with fits, are shown in comparison to a curve from a conventional, diffraction-limited volume. The fits, for which the only free parameter is the waveguide diameter, show excellent agreement with the data. The average residence times for molecules in the effective observation volume of zero-mode waveguides, as measured at the point where $G(\tau)$ is 0.5, are only a few microseconds, an order of magnitude faster than that for the diffraction-limited case and three orders of magnitude faster than many enzymatic reaction rates. This large difference in time scales is important for distinguishing a molecule that diffuses into the observation volume from a ligand in the active site of an enzyme adsorbed onto the bottom of the waveguide.

We have used zero-mode waveguides to observe the enzymatic synthesis of double stranded DNA by DNA polymerase with the use of the fluorescently tagged nucleotide analog coumarin-dCTP in place of dCTP (30). The

equilibrium dissociation constants of nucleotides for most polymerases are above 1 μM (31); therefore, fast and efficient DNA synthesis only occurs at those or higher concentrations. We immobilized mutant T7 DNA polymerases in the waveguides at a density such that only a fraction of all zero-mode waveguides would contain an active polymerase. After a washing step to remove unbound enzymes and subsequent incubation with a reaction mixture supporting efficient and processive synthesis of M13 DNA (including 7.5 μM coumarin-dCTP instead of dCTP), we observed bursts of fluorescence with a duration of ~ 1 to 100 ms from individual waveguides (Fig. 4C). This activity was only observed when all reagents necessary to support DNA synthesis were present. Furthermore, burst activities stopped in all waveguides after ~ 30 min, consistent with control experiments that showed that synthesis of the complementary strand of M13 DNA by immobilized polymerase was completed by that time. Our interpretation that these bursts stem from enzymatic incorporation of coumarin-dCTP into DNA, followed by photobleaching of the fluorophore, is also supported by the fact that the average duration of fluorescence from the incorporated analog in the waveguide depended on illumination intensity (Fig. 4D, blue curve). The observed burst frequency of 1 to 3 bursts per second (Fig. 4C) is in good agreement with the value expected from the average rate of DNA synthesis measured in bulk solution (~ 10 to 15 bases per second) and the average content of $\sim 20\%$ guanine in the template. Using templates with regular, periodic base distributions or with replacement of more than one base type by fluorescent nucleotide analogs for obtaining sequence information (32) would enable more precise determination of single-molecule enzymatic rates and rate fluctuations.

We anticipate that the ability to carry out single-molecule analysis at high concentrations will find wide applicability in FCS, cross-correlation, and other spectroscopic techniques. Because the optical intensity and the output coupling efficiency at the entrance of the waveguide are close to those for free space, zero-mode waveguides offer an optically efficient, highly parallel, and relatively simple platform for performing a wide variety of biochemical assays.

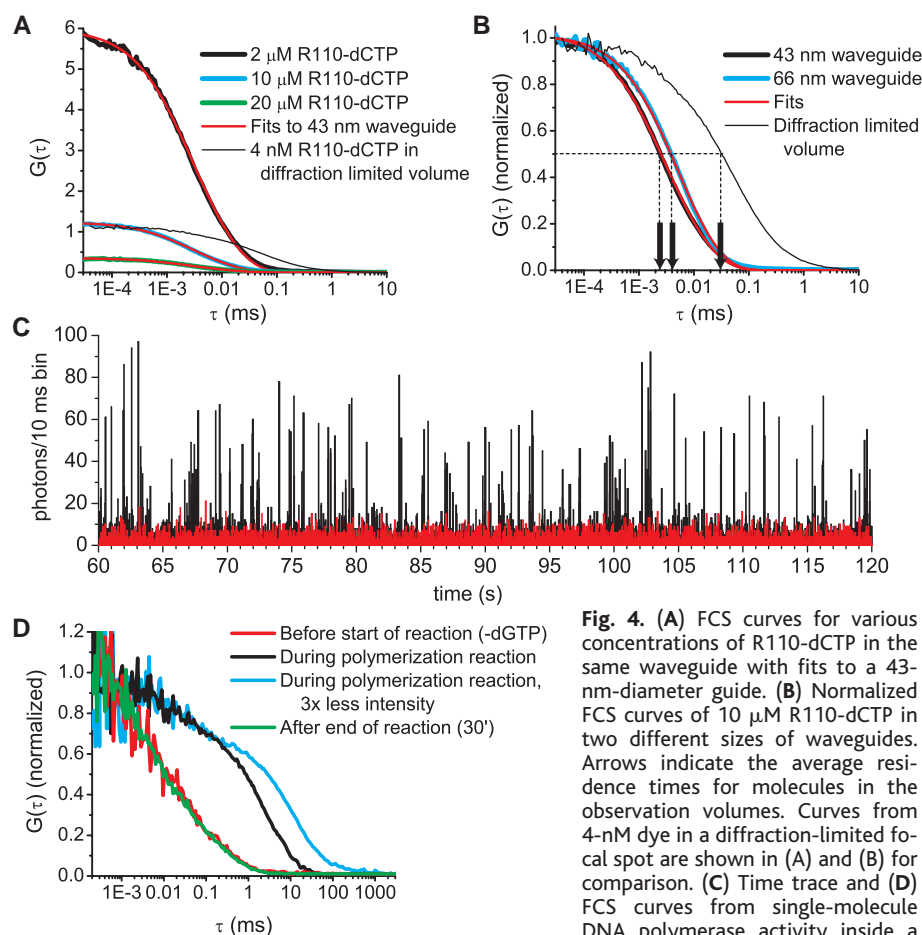


Fig. 4. (A) FCS curves for various concentrations of R110-dCTP in the same waveguide with fits to a 43-nm-diameter guide. (B) Normalized FCS curves of 10 μM R110-dCTP in two different sizes of waveguides. Arrows indicate the average residence times for molecules in the observation volumes. Curves from 4-nM dye in a diffraction-limited focal spot are shown in (A) and (B) for comparison. (C) Time trace and (D) FCS curves from single-molecule DNA polymerase activity inside a zero-mode waveguide. Incorporation

events and subsequent photobleaching of coumarin-dCTP appear as distinct fluorescence bursts in the black time trace (10-ms time bins). This results in a long-time shoulder in the corresponding FCS curves during polymerization (black and blue curves) in (D). Decreasing the intensity results in slower photobleaching as seen by the longer residence time in the blue curve. The red curves in (C) and (D) are the corresponding negative controls (absence of one native nucleotide) in the same waveguide before initiation of the reaction. The green curve in (D) is the control after the reaction has stopped.

References and Notes

- X. S. Xie, H. P. Lu, *J. Biol. Chem.* **274**, 15967 (1999).
- H. P. Lu, L. Xun, X. S. Xie, *Science* **282**, 1877 (1998).
- A. Castro, J. G. Williams, *Anal. Chem.* **69**, 3915 (1997).
- R. A. Keller et al., *Anal. Chem.* **74**, 316A (2002).
- A. T. Woolley, C. Guillemette, C. Li Cheung, D. E. Housman, C. M. Lieber, *Nature Biotechnol.* **18**, 760 (2000).
- D. Magde, E. Elson, W. W. Webb, *Phys. Rev. Lett.* **29**, 705 (1972).
- J. Mertz, C. Xu, W. W. Webb, *Optics Lett.* **20**, 2532 (1995).
- L. S. Barak, W. W. Webb, *J. Cell Biol.* **90**, 595 (1981).
- M. A. Medina, P. Schwill, *Bioessays* **24**, 758 (2002).
- F. J. Meyer-Almes, M. Auer, *Biochemistry* **39**, 13261 (2000).

11. D. Schomburg, I. Schomburg, *Springer Handbook of Enzymes* (Springer, New York, ed. 2, 2001).
12. H. P. Lerch, A. S. Mikhailov, B. Hess, *Proc. Natl. Acad. Sci. U.S.A.* **99**, 15410 (2002).
13. T. E. Starr, N. L. Thompson, *Biophys. J.* **80**, 1575 (2001).
14. F. de Lange et al., *J. Cell Sci.* **114**, 4153 (2001).
15. E. Betzig, R. J. Chichester, *Science* **262**, 1422 (1993).
16. D. R. Reyes, D. Iossifidis, P.-A. Auroux, A. Manz, *Anal. Chem.* **74**, 2623 (2002).
17. P.-A. Auroux, D. Iossifidis, D. R. Reyes, A. Manz, *Anal. Chem.* **74**, 2637 (2002).
18. H. G. Craighead, *Science* **290**, 1532 (2000).
19. J. D. Jackson, *Classical Electrodynamics* (Wiley & Sons, New York, ed. 3, 1999).
20. K. Rippe, *Biochemistry* **39**, 2131 (2000).
21. J. Ricka, T. Binkert, *Phys. Rev. A* **39**, 2646 (1989).
22. Materials and methods are available as supporting material on Science Online.
23. D. Kleppner, *Phys. Rev. Lett.* **47**, 233 (1981).
24. E. M. Purcell, *Phys. Rev.* **69**, 681 (1946).
25. E. Yablonivitch, *Phys. Rev. Lett.* **58**, 2059 (1987).
26. C. Xu, W. W. Webb, in *Topics in Fluorescence Spectroscopy*, vol. 5, *Nonlinear and Two-Photon-Induced Fluorescence*, J. Lakowicz, Ed. (Plenum Press, New York, 1997), pp. 471–540.
27. E. L. Elson, D. Magde, *Biopolymers* **13**, 1 (1974).
28. N. L. Thompson, T. P. Burghardt, D. Axelrod, *Biophys. J.* **33**, 435 (1981).
29. D. E. Koppel, *Phys. Rev. A* **10**, 1938 (1974).
30. Coumarin-dCTP was found to be efficiently and processively incorporated into DNA by Sequenase (USB Corporation, Cleveland, OH), a mutant T7 DNA polymerase. Detailed reaction conditions are given in (22).
31. S. S. Patel, I. Wong, K. A. Johnson, *Biochemistry* **30**, 511 (1991).
32. J. Korlach et al., Patent Cooperation Treaty International Application No. WO 0070073, Cornell Research Foundation (2000).
33. We thank K. Hodgson for Fig. 1, M. Isaacson for obtaining Fig. 3D, and Amersham Biosciences for providing

R110-dCTP. Supported by grant DE-FG02-99ER62809 from the U.S. Department of Energy. Additional support was received from NSF grant DBI-0080792 and from the facilities of National Center for Research Resources—NIH Biomedical Technology Resource, grant P41-RR04224, and the Nanobiotechnology Center, NSF—Science and Technology Center grant agreement ECS-9876771. Device fabrication was performed at the Cornell Nanofabrication Facility.

Supporting Online Material

www.sciencemag.org/cgi/content/full/299/5607/682/DC1

Materials and Methods

SOM Text

Figs. S1 and S2

Movies S1 and S2

23 October 2002; accepted 12 December 2002

Nitriding Iron at Lower Temperatures

W. P. Tong,¹ N. R. Tao,¹ Z. B. Wang,¹ J. Lu,² K. Lu^{1*}

The microstructure in the surface layer of a pure iron plate was refined at the nanometer scale by means of a surface mechanical attrition treatment that generates repetitive severe plastic deformation of the surface layer. The subsequent nitriding kinetics of the treated iron with the nanostructured surface layer were greatly enhanced, so that the nitriding temperature could be as low as 300°C, which is much lower than conventional nitriding temperatures (above 500°C). This enhanced processing method demonstrates the technological significance of nanomaterials in improving traditional processing techniques and provides a new approach for selective surface reactions in solids.

Most surface-modification techniques used for solid materials are based on various chemical reactions that produce optimized structure and properties in order to improve the global performance of the materials. However, widespread uses of these techniques are frequently hindered by the reaction kinetics involved. For example, nitriding is a chemical treatment widely used to form surface nitrides. This technique is of great industrial interest, because it forms a unique composite structure with a hard surface (a layer of Fe-nitride compounds) and a tough interior, so that the global mechanical performance and wear/corrosion resistance of alloys and steels can be greatly improved (1). However, nitriding processes are performed at high temperatures (>500°C) for a long duration (~20 to 80 hours) (1, 2) and may induce serious deterioration of the substrate in many families of materials.

A change of the surface microstructure by means of grain refinement is one option that can be used to accelerate the chemical reaction of a

material surface. It is known that nanocrystalline materials possess ultrafine grains with a large number of grain boundaries that may act as fast atomic diffusion channels (3, 4). Greatly enhanced atomic diffusivities in nanocrystalline materials relative to their conventional coarse-grained counterparts have been experimentally observed (5, 6). A large number of grain boundaries with various kinds of nonequilibrium defects also constitutes a high excess stored energy that may further facilitate their chemical reactivity. It has been demonstrated experimentally that chemical reaction (or phase transformation) kinetics are greatly enhanced during mechanical attrition of solids, in which the grain size is

significantly reduced to the nanometer scale and structural defects are created by the severe plastic deformation (7–9). Nitriding of iron was observed when Fe powders were processed in situ by ball-milling in a nitrogen-containing atmosphere at nominal ambient temperature (10, 11), although a considerable transient temperature rise (as high as a few hundred degrees) always accompanies the impacts of the milling balls and may have contributed to an enhanced chemical reactivity.

We demonstrate enhanced chemical reaction kinetics at lower temperatures when the surface layer of a metal is transformed into a nanocrystalline structure, using the nitriding of Fe as an example. Our experimental observations show that surface nanocrystallization greatly facilitates the nitriding process, and it thus provides an alternative approach to surface modification of metallic materials.

A surface layer with nanocrystalline grains can be produced on a bulk metal by using a recently developed surface mechanical attrition treatment (SMAT) (12–14). The basic principle of the treatment is the generation of plastic deformation in the top surface layer of a bulk material by means of repeated multidirectional impacts of flying balls on the sample surface (Fig. 1A). The plastic deformation in the surface layer with a large strain and a high strain rate results in a progressive refinement of coarse grains into the nanometer regime. Stainless steel balls (with a mirrorlike surface and a diameter of

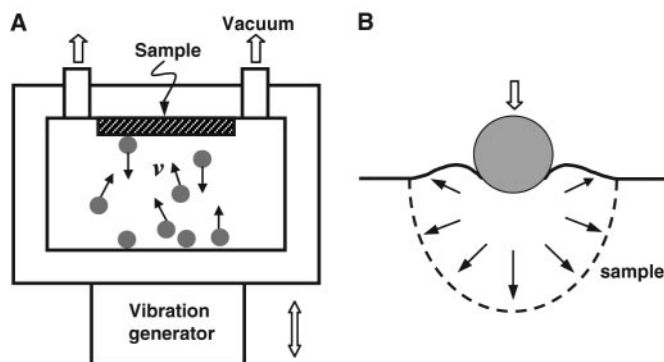


Fig. 1. Schematic illustrations of (A) the SMAT technique and (B) the localized plastic deformation zone induced by the vibrating ball.

¹Shenyang National Laboratory for Materials Science, Institute of Metal Research, Chinese Academy of Sciences, Shenyang 110016, China. ²Laboratoire des Systèmes Mécaniques et d'Ingénierie Simultanée (LASMIS), University of Technology of Troyes, 10000, Troyes, France.

*To whom correspondence should be addressed. E-mail: lu@imr.ac.cn